

WHEN GEOMETRY ALIGNS: DIHEDRAL HIDDEN-STATE TRANSFORMATIONS IN UNET, ViT, AND DiT ARCHITECTURES.

Mojtaba Faramarzi

University of Montreal, Canada
Mila - Quebec AI Institute

Alex Lamb *

Tsinghua University
China

Irina Rish *

University of Montreal, Canada
Mila - Quebec AI Institute

ABSTRACT

Diffusion architectures now encompass convolutional UNets as well as transformer-based designs such as Diffusion Transformers (DiTs), inspired by Vision Transformers (ViTs), yet the effects of structured geometric perturbations within these architectures remain poorly understood. We study this question through a unified framework that applies reflection-based elements of the dihedral group to intermediate hidden states as controlled internal interventions, contrasting geometrically consistent and inconsistent variants. Using activation-level diagnostics, including Self-Consistency Shift (SCS), Activation Mass Scatter (AMS), and Drift, we analyze feature stability and geometric drift. We find that consistent transformations improve stability, while inconsistent ones induce predictable, architecture-specific failures. In the main Stable Diffusion 2.1 U-Net study, we evaluate seven intervention modes over three seeds and complement the internal diagnostics with image-level FID, KID, CLIP score, and LPIPS diversity. Taken together with supporting ViT and controlled DiT analyses, these results establish geometric consistency as a key principle for stable hidden-state interventions in spatially structured vision and diffusion models.

1 INTRODUCTION

Modern machine learning systems are increasingly modified during or after training through fine-tuning, parameter-efficient adaptation, internal editing, feature-level perturbations, and other forms of hidden-state intervention (Vaswani et al., 2017; Hu et al., 2021; Meng et al., 2022). In vision and generative modeling, such interventions are applied to architectures whose intermediate representations carry strong spatial structure, including convolutional U-Nets and transformer-based models such as ViTs and DiTs (Dosovitskiy et al., 2021; Touvron et al., 2021; Peebles & Xie, 2023; Ho et al., 2020; Song et al., 2021a;b; Rombach et al., 2022). This raises a basic but underexplored question: what makes an internal geometric transformation compatible with the computation of a spatially structured model?

Prior work has studied input and latent-space augmentation and robustness (Shorten & Khoshgoftaar, 2019; Zhang et al., 2018; Yun et al., 2019; Faramarzi et al., 2022), architectural equivariance and symmetry-aware modeling (Cohen & Welling, 2016; Weiler et al., 2018; Finzi et al., 2021; Hoogeboom et al., 2022), and hidden-state manipulation for interpretation, control, and editing (Geva et al., 2021; Dai et al., 2021; Hertz et al., 2022; Meng et al., 2022; Chefer et al., 2021; Bau et al., 2017). However, modern diffusion and vision backbones have not been systematically studied from the perspective of *hidden-state geometric interventions*: structured transformations applied directly to intermediate representations inside otherwise standard architectures. This setting is especially informative because it reveals whether a model can accommodate internal geometric change while preserving the spatial organization of its features.

In this work, we study dihedral hidden-state transformations as controlled internal interventions in U-Net-, ViT-, and DiT-style models. Our contributions are fourfold. First, we introduce a unified framework for applying hidden-state geometric transformations across convolutional and transformer-based architectures. Second, we develop a theoretical framework that formalizes hidden-state geometric interventions and explains geometric consistency as the condition under which such interventions preserve coherent computation. Third, we introduce activation-level diagnostics that we term Self-Consistency Shift (SCS), Activation Mass Scatter (AMS), and Drift, together with a fidelity-oriented proxy metric. Fourth, empirically, we conduct a main quantitative study on the Stable Diffusion 2.1 U-Net, complemented by supporting ViT and controlled DiT analyses, and show that geometrically consistent interventions improve internal stability whereas inconsistent interventions induce structured misalignment.

* Equal Supervision.

Using these diagnostics, our main U-Net study shows that geometrically consistent interventions improve feature stability, whereas inconsistent interventions lead to systematic geometric mismatch and reduced fidelity.

2 METHOD: GEOMETRIC HIDDEN-STATE INTERVENTIONS

We study *hidden-state interventions* that apply a spatial transformation directly to an intermediate representation inside a vision or diffusion architecture. Let $z^{(\ell)}$ denote the hidden state at layer or block ℓ , and let T denote a spatial transformation. Although the dihedral group D_4 contains both rotations and reflections, the implemented transform set in this work is the reflection subset $\mathcal{T} = \{T_{\text{hor}}, T_{\text{ver}}, T_{\text{diag}}, T_{\text{anti}}\} \subset D_4$, namely horizontal, vertical, main-diagonal, and anti-diagonal flips. Accordingly, our empirical claims apply to this reflection-based instantiation; extending the analysis to rotations is left for future work. This choice isolates the effect of internal geometric change while keeping the underlying architecture fixed. Our central question is whether such an intervention preserves the spatial frame expected by the downstream computation.

Our organizing principle is *geometric consistency*. An intervention is *consistent* if all interacting components that consume the transformed representation operate in the same spatial frame. It is *inconsistent* if the transformation is applied to only part of a coupled computation, so that different branches operate in incompatible coordinate systems. This principle is the main lens through which we analyze both attention-based architectures and U-Net-style feature hierarchies. In multi-head attention, the coupled computation arises from the interaction of token routing within each head and the subsequent mixing of heads through output projection (Vaswani et al., 2017). In U-Net backbones, it appears through skip-connected encoder–decoder fusion (Ronneberger et al., 2015) and attention blocks embedded inside diffusion architectures (Ho et al., 2020; Rombach et al., 2022). In both settings, hidden-state interventions remain well-posed only when all coupled pathways stay geometrically aligned.

2.1 TRANSFORMER INTERVENTION: FLIPPED-HEAD ATTENTION

Consider a transformer block with input token matrix $X \in \mathbb{R}^{N \times d_{\text{model}}}$, where $N = P^2$ tokens are arranged on a $P \times P$ patch grid, as in Vision Transformers (Dosovitskiy et al., 2021). For head h , standard self-attention is (Vaswani et al., 2017)

$$Q_h = XW_h^Q, \quad K_h = XW_h^K, \quad V_h = XW_h^V, \quad O_h = \alpha_h V_h, \quad \alpha_h = \text{softmax}\left(\frac{Q_h K_h^\top}{\sqrt{d_k}}\right). \quad (1)$$

The multi-head output is

$$Y = \text{Concat}(O_1, \dots, O_H)W^O.$$

We intervene on a selected head h^* by reshaping its output into

$$\mathcal{O}_{h^*} \in \mathbb{R}^{P \times P \times d_v}, \quad \mathcal{O}_{h^*}[i, j, :] = O_{h^*}[t(i, j), :],$$

where $t(i, j) = (i - 1)P + j$, applying a spatial transformation T , and then flattening back. For example, for a horizontal flip,

$$(T\mathcal{O}_{h^*})[i, j, :] = \mathcal{O}_{h^*}[i, P - j + 1, :]. \quad (2)$$

Let $\tilde{\mathcal{O}}_{h^*}$ denote the flattened transformed output. The intervened multi-head representation is then

$$\hat{O} = \text{Concat}(O_1, \dots, O_{h^*-1}, \tilde{\mathcal{O}}_{h^*}, O_{h^*+1}, \dots, O_H), \quad Y = \hat{O}W^O. \quad (3)$$

A detailed derivation is provided in Appendix A.

Attention-Consistent and Attention-Inconsistent Variants. Let $\mathcal{A}(Q, K, V) = \text{softmax}\left(\frac{QK^\top}{\sqrt{d_k}}\right)V$ denote the attention output of a single head, and let Π_T be the permutation matrix induced by the spatial transformation T on token indices. A geometrically consistent transformation of a single head satisfies

$$\mathcal{A}(\Pi_T Q, \Pi_T K, \Pi_T V) = \Pi_T \mathcal{A}(Q, K, V), \quad (4)$$

so token routing and aggregation remain in a common transformed frame.

In our setting, the relevant inconsistency arises not at the level of an isolated head, but at the level of the full multi-head module. If only one selected head h^* is transformed after attention, the module output becomes

$$Y_{\text{inc}} = \text{Concat}(O_1, \dots, \Pi_T \mathcal{O}_{h^*}, \dots, O_H)W^O, \quad (5)$$

which mixes transformed and untransformed heads before output projection. In contrast, a geometrically consistent transformation applies the same spatial map to all interacting heads:

$$Y_{\text{cons}} = \text{Concat}(\Pi_T O_1, \dots, \Pi_T O_H) W^O = \Pi_T \text{Concat}(O_1, \dots, O_H) W^O. \quad (6)$$

The second equality holds because Π_T acts on the token axis, whereas W^O acts only on channel features. Thus, the crucial distinction is not whether a flip is applied, but whether the interacting heads remain expressed in a common geometric frame. In iterative transformer denoisers such as DiT, this mismatch can compound across denoising steps and manifest as increased drift and reduced stability. Full proofs and the timestep-sensitivity analysis are deferred to Appendix B.

2.2 RANDOM HIDDEN-STATE GEOMETRIC AUGMENTATION

The transformer construction above motivates a broader intervention scheme: rather than applying a fixed transformation to a single head, we consider stochastic hidden-state transformations applied at arbitrary intermediate locations. Let $\mathcal{T} = \{T_{\text{hor}}, T_{\text{ver}}, T_{\text{diag}}, T_{\text{anti}}\}$, where the elements denote horizontal, vertical, main-diagonal, and anti-diagonal reflections. For a selected block ℓ with hidden state $H^{(\ell)}$, we sample an intervention pair (ℓ, τ) with $\tau \in \mathcal{T}$ and apply

$$\tilde{H}^{(\ell)} = \tau(H^{(\ell)}). \quad (7)$$

In our implementation, exactly one intervention location is selected per mini-batch. This yields a lightweight hidden-state augmentation scheme that exposes the model to multiple geometric views while remaining compatible with pretrained backbones and requiring no architectural redesign. The same consistency principle applies at this more general level: once a hidden state is transformed, all downstream computations that interact through that state must remain in a common spatial frame. We next make this explicit for diffusion models.

2.3 HIDDEN-STATE INTERVENTION IN DIFFUSION MODELS

We now instantiate the same principle for diffusion denoisers, including both U-Net-based architectures (Ronneberger et al., 2015; Ho et al., 2020; Rombach et al., 2022) and transformer-based denoisers such as DiT (Peebles & Xie, 2023). In both cases, we apply a spatial transformation to an intermediate hidden state during denoising and train the model to remain stable under this intervention.

Let $x_0 \sim p_{\text{data}}$ be a clean training sample, $\varepsilon \sim \mathcal{N}(0, I)$, and x_t the noisy sample at diffusion step t . Let $\varepsilon_\theta(x_t, t)$ denote the denoiser. For a chosen layer or block ℓ , let $F^{(\ell)}(x_t, t) \in \mathbb{R}^{C_\ell \times H_\ell \times W_\ell}$ denote the corresponding hidden activation. Given a sampled transformation $\tau \in \mathcal{T}$, we define the transformed hidden state

$$\tilde{F}^{(\ell)}(x_t, t) = \tau\left(F^{(\ell)}(x_t, t)\right). \quad (8)$$

Let $\varepsilon_\theta^{(\tau, \ell)}(x_t, t)$ denote the denoiser output obtained by running the network up to block ℓ , replacing $F^{(\ell)}(x_t, t)$ by $\tilde{F}^{(\ell)}(x_t, t)$, and propagating the modified activation through the remainder of the network. The corresponding training objective is

$$\mathcal{L}_{\text{aug}}(\theta) = \mathbb{E}_{x_0, \varepsilon, t, \ell, \tau} \left[\|\varepsilon - \varepsilon_\theta^{(\tau, \ell)}(x_t, t)\|_2^2 \right]. \quad (9)$$

This objective is shared across both U-Net and DiT backbones; what differs is how geometric consistency is realized by the underlying architecture. In a U-Net, the critical interaction arises at skip-connected encoder–decoder fusion. Consider a skip pair (ℓ, ℓ') whose encoder and decoder features have the same spatial resolution. Let $F_{\text{enc}}^{(\ell)} \in \mathbb{R}^{C_{\text{enc}} \times H \times W}$ denote the encoder feature map, and let $F_{\text{dec}}^{(\ell')} \in \mathbb{R}^{C_{\text{dec}} \times H \times W}$ denote the corresponding decoder feature map. Let ϕ denote the skip-fusion operator that combines these two tensors into a single representation; for example, ϕ may be concatenation followed by a shared convolution, or any other fusion map used by the architecture. We write the fused feature as

$$G^{(\ell, \ell')} = \phi\left(F_{\text{dec}}^{(\ell')}, F_{\text{enc}}^{(\ell)}\right). \quad (10)$$

A geometrically consistent intervention applies the same transformation to both coupled branches before fusion:

$$\tilde{G}^{(\ell, \ell')} = \phi\left(\tau(F_{\text{dec}}^{(\ell')}), \tau(F_{\text{enc}}^{(\ell)})\right). \quad (11)$$

By contrast, transforming only one branch, for example

$$\phi\left(\tau(F_{\text{dec}}^{(\ell')}), F_{\text{enc}}^{(\ell)}\right) \quad \text{or} \quad \phi\left(F_{\text{dec}}^{(\ell')}, \tau(F_{\text{enc}}^{(\ell)})\right),$$

creates a skip inconsistency by fusing features expressed in different spatial frames.

In DiT-style transformer denoisers, the same objective in Eq. 9 applies, but the coupled computation is formed by attention and token mixing rather than skip fusion. As in the transformer case above, geometric consistency requires all interacting attention pathways to share the same transformed frame; partial transformations instead create cross-head or cross-branch mismatch. Thus, the same geometric-consistency principle governs both U-Net and DiT diffusion models: hidden-state interventions remain stable only when all coupled computations stay geometrically aligned. Additional implementation details are deferred to Appendix C.

3 THEORETICAL ANALYSIS: STABILITY AND REGULARIZATION UNDER GEOMETRIC CONSISTENCY

The method section defines how hidden-state transformations are applied, but not why consistent interventions remain stable while inconsistent ones induce mismatch. This section addresses that gap by characterizing flipped-head representations, formalizing consistency in attention and U-Net fusion, and giving an idealized regularization interpretation of symmetry-consistent interventions.

3.1 REPRESENTATION INDUCED BY A FLIPPED HEAD

We begin with the simplest symmetric geometric intervention considered in the paper: a horizontal flip applied to the output of a selected attention head. The following result characterizes the spatial correspondence induced by this operation.

Lemma 3.1 (Flip-induced spatial correspondence). *Let h^* be the selected head, and let \tilde{O}_{h^*} denote the flattened output obtained by horizontally flipping the reshaped head output. Then, for every spatial position (i, j) ,*

$$\tilde{O}_{h^*}[t(i, j), :] = O_{h^*}[t(i, P - j + 1), :]. \quad (12)$$

Proof. See Appendix D.1.

We next expand how this intervention appears in the final multi-head token representation.

Proposition 3.2 (Final token representation with a flipped head). *Let $W^O = [W_1^O \cdots W_H^O]$ be partitioned into head-wise blocks, with $W_h^O \in \mathbb{R}^{d_{\text{model}} \times d_v}$, and let $o_h[t] := O_h[t, :]^\top \in \mathbb{R}^{d_v}$ denote the token feature of head h at token index t . Then, for each spatial location (i, j) ,*

$$y_{t(i, j)} = \sum_{h \neq h^*} W_h^O o_h[t(i, j)] + W_{h^*}^O o_{h^*}[t(i, P - j + 1)]. \quad (13)$$

Proof. See Appendix D.2.

Proposition 3.2 shows that the flipped-head intervention injects mirrored contextual information into the token representation while leaving all remaining heads anchored at the original spatial location.

3.2 CONSISTENCY PRINCIPLES FOR ATTENTION AND U-NET FUSION

We next formalize why consistency is necessary inside attention. At the level of an isolated head, a shared spatial transformation preserves equivariance. The inconsistency in our setting arises instead at the level of the full multi-head module: if only part of the interacting computation is transformed, the output projection mixes representations expressed in different geometric frames.

Proposition 3.3 (Attention consistency under a shared spatial transformation). *Let $Y = \text{Concat}(O_1, \dots, O_H)W^O$, and let Π_T denote the permutation induced by a spatial transformation T on token indices. If all head outputs are transformed by the same Π_T , then*

$$Y_{\text{cons}} = \text{Concat}(\Pi_T O_1, \dots, \Pi_T O_H)W^O = \Pi_T Y. \quad (14)$$

By contrast, if only a strict subset of heads is transformed, then in general the resulting module output cannot be written as $\Pi_T Y$.

Proof. See Appendix D.3.

An analogous principle holds for U-Net feature fusion, where the interacting paths are the branches entering a skip-connected fusion operator.

Proposition 3.4 (Skip consistency under simultaneous transformation). *Consider a skip pair (ℓ, ℓ') at matched spatial resolution, with encoder feature map $F_{\text{enc}}^{(\ell)} \in \mathbb{R}^{C_{\text{enc}} \times H \times W}$ and decoder feature map $F_{\text{dec}}^{(\ell')} \in \mathbb{R}^{C_{\text{dec}} \times H \times W}$. Let $G^{(\ell, \ell')} = \phi(F_{\text{dec}}^{(\ell')}, F_{\text{enc}}^{(\ell)})$ be the fused representation, where $\phi : \mathbb{R}^{C_{\text{dec}} \times H \times W} \times \mathbb{R}^{C_{\text{enc}} \times H \times W} \rightarrow \mathbb{R}^{C_{\text{out}} \times H \times W}$ is a skip-fusion operator. Assume that ϕ is equivariant under simultaneous spatial permutation, i.e.*

$$\phi(\Pi_T a, \Pi_T b) = \Pi_T \phi(a, b).$$

Then transforming both branches by the same Π_T preserves a common transformed frame:

$$\phi(\Pi_T F_{\text{dec}}^{(\ell')}, \Pi_T F_{\text{enc}}^{(\ell)}) = \Pi_T \phi(F_{\text{dec}}^{(\ell')}, F_{\text{enc}}^{(\ell)}). \quad (15)$$

Transforming only one branch generally does not preserve this relation and thus introduces geometric mismatch at fusion.

Proof. See Appendix D.4.

Together, Propositions 3.3 and 3.4 explain the mismatch patterns observed in the experiments: stable interventions preserve geometric alignment, whereas partial transformations introduce structured inconsistency across interacting computations.

3.3 SYMMETRY CONSTRAINTS AS REGULARIZATION

Beyond stability, geometric consistency also admits an idealized statistical interpretation. Let \mathcal{H} be a hypothesis class of predictors $h : \mathcal{X} \rightarrow \mathbb{R}$, and let $T : \mathcal{X} \rightarrow \mathcal{X}$ be a symmetry transformation. We define the symmetry-constrained subclass $\mathcal{H}_{\text{sym}} = \{h \in \mathcal{H} : h(x) = h(T(x)) \text{ for all } x \in \mathcal{X}\}$. By construction, $\mathcal{H}_{\text{sym}} \subseteq \mathcal{H}$. Now let $S = \{x_i\}_{i=1}^n$ be a sample, and let $\sigma_1, \dots, \sigma_n \stackrel{\text{i.i.d.}}{\sim} \text{Unif}\{-1, +1\}$ denote Rademacher random variables. The empirical Rademacher complexity of a scalar-valued function class \mathcal{F} is

$$\widehat{\mathcal{R}}_S(\mathcal{F}) = \mathbb{E}_\sigma \left[\sup_{f \in \mathcal{F}} \frac{1}{n} \sum_{i=1}^n \sigma_i f(x_i) \right]. \quad (16)$$

Since $\mathcal{H}_{\text{sym}} \subseteq \mathcal{H}$, monotonicity gives $\widehat{\mathcal{R}}_S(\mathcal{H}_{\text{sym}}) \leq \widehat{\mathcal{R}}_S(\mathcal{H})$. To connect this to generalization, let $\psi : \mathbb{R} \times \mathcal{Y} \rightarrow [0, 1]$ be a loss function that is L -Lipschitz in its first argument, and define the induced loss class

$$\mathcal{L}_{\mathcal{H}} = \{(x, y) \mapsto \psi(h(x), y) : h \in \mathcal{H}\}.$$

Since $\mathcal{H}_{\text{sym}} \subseteq \mathcal{H}$, we also have $\mathcal{L}_{\mathcal{H}_{\text{sym}}} \subseteq \mathcal{L}_{\mathcal{H}}$. Therefore, $\widehat{\mathcal{R}}_S(\mathcal{L}_{\mathcal{H}_{\text{sym}}}) \leq \widehat{\mathcal{R}}_S(\mathcal{L}_{\mathcal{H}})$. A standard Rademacher-complexity bound then implies that, with probability at least $1 - \delta$ over a sample $S = \{(x_i, y_i)\}_{i=1}^n$,

$$\mathcal{E}(h) \leq \widehat{\mathcal{E}}_S(h) + 2\widehat{\mathcal{R}}_S(\mathcal{L}_{\mathcal{H}}) + 3\sqrt{\frac{\log(2/\delta)}{2n}}, \quad (17)$$

where $\mathcal{E}(h)$ and $\widehat{\mathcal{E}}_S(h)$ denote the population and empirical risks, respectively (Bartlett & Mendelson, 2002). Applying the same bound to the symmetry-constrained subclass, equivalently to the induced loss class $\mathcal{L}_{\mathcal{H}_{\text{sym}}}$, yields a no-larger complexity term. This provides an idealized interpretation of symmetry-consistent hidden-state augmentation as a form of capacity-reducing regularization. A proof of the monotonicity argument is provided in Appendix D.5. This argument is idealized and is intended to explain the regularizing effect of symmetry constraints at the level of function classes, rather than as a formal generalization theorem for the full diffusion training pipeline. This argument establishes monotonicity of the complexity term, but does not quantify the magnitude of the reduction, which depends on how restrictive the symmetry constraint is for the underlying hypothesis class.

4 EXPERIMENTS

We evaluate geometric hidden-state interventions through a main empirical study on the Stable Diffusion 2.1 U-Net, complemented by additional experiments on other diffusion backbones, FID-based comparisons, and supporting synthetic and transformer analyses.

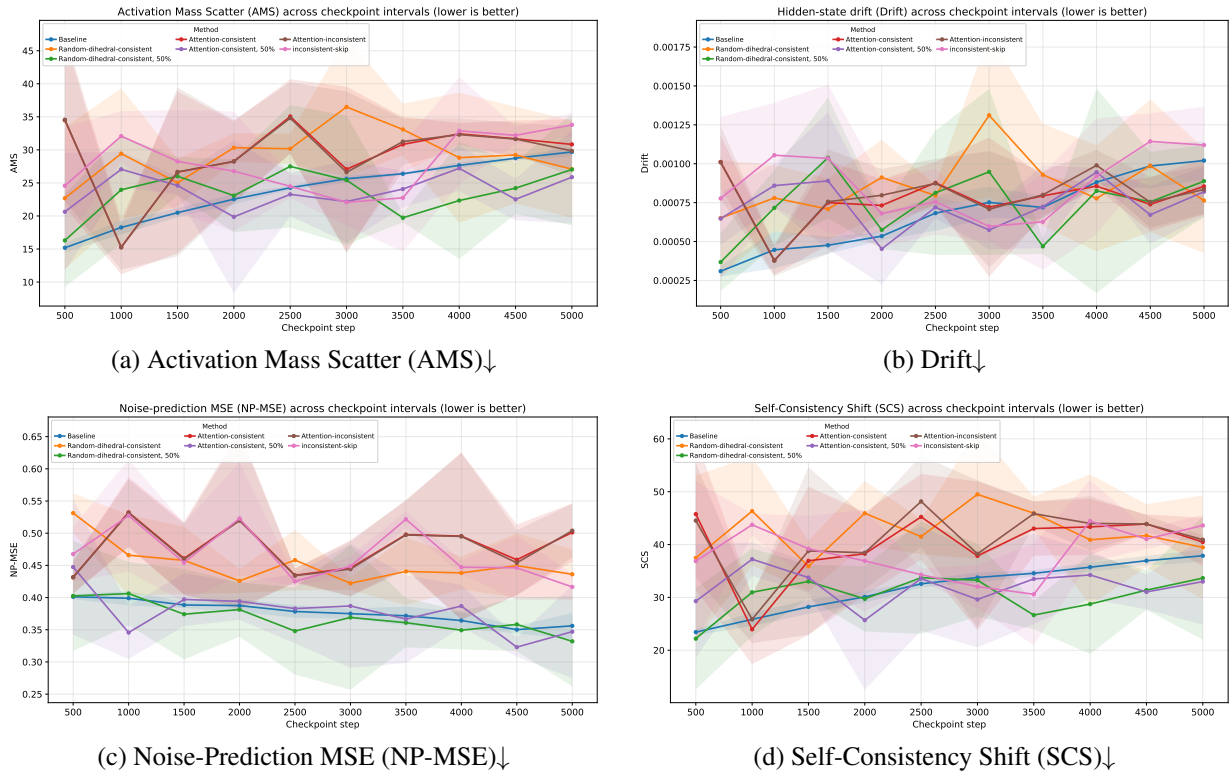


Figure 1: Quantitative evaluation over 5,000 steps for seven modes, averaged over three seeds (lower values are better).

4.1 PRIMARY EXPERIMENTAL TESTBED

As one controlled text-to-image testbed, we use the Stable Diffusion 2.1 U-Net, fine-tuned under a unified intervention framework that applies one sampled geometric transformation at one sampled location per forward pass. We train seven modes: *baseline*, *random-dihedral-consistent*, *attention-consistent*, their 50% variants, and two inconsistent controls, *attention-inconsistent* and *inconsistent-skip*. In the 50% variants, the intervention is applied to a random half of minibatches; the remaining minibatches use the clean baseline update. Depending on the mode, interventions are applied at ResNet blocks, attention blocks, or skip-fusion locations. For controlled experiments, we use 500 randomly sampled Oxford-IIIT Pet images resized to 512×512 and fine-tune for 5,000 steps over three seeds. Additional details are deferred to Appendices E and F.

We use Oxford-IIIT Pet as a controlled natural-image testbed with a clear cat/dog split and diverse pose, texture, and background variation. We use the same random 500-image subset for all modes to keep the seven-mode, three-seed comparison tractable and controlled.

4.2 EVALUATION METRICS

We evaluate both denoising fidelity and internal geometric stability using four metrics: *Noise-Prediction Mean Squared Error (NP-MSE)*, *Self-Consistency Shift (SCS)*, *Activation Mass Scatter (AMS)*, and *Drift*. The first measures noise-prediction fidelity, while the latter three quantify complementary aspects of hidden-state stability under intervention. Lower values are better for all metrics.

Noise-Prediction MSE (NP-MSE). Because full Fréchet Inception Distance (FID) requires large-scale image generation and an additional Inception-network pass, we use a lightweight fidelity proxy based on the standard diffusion noise-prediction error:

$$\text{NP-MSE} = \mathbb{E}_{x_t, t} [\|\hat{\varepsilon}_\theta(x_t, t) - \varepsilon\|_2^2]. \quad (18)$$

Here, x_t denotes the noisy latent at diffusion step t , ε the injected noise, and $\hat{\varepsilon}_\theta(x_t, t)$ the model prediction. Lower values indicate better denoising performance. Despite the shorthand name, this metric is simply the denoising noise-

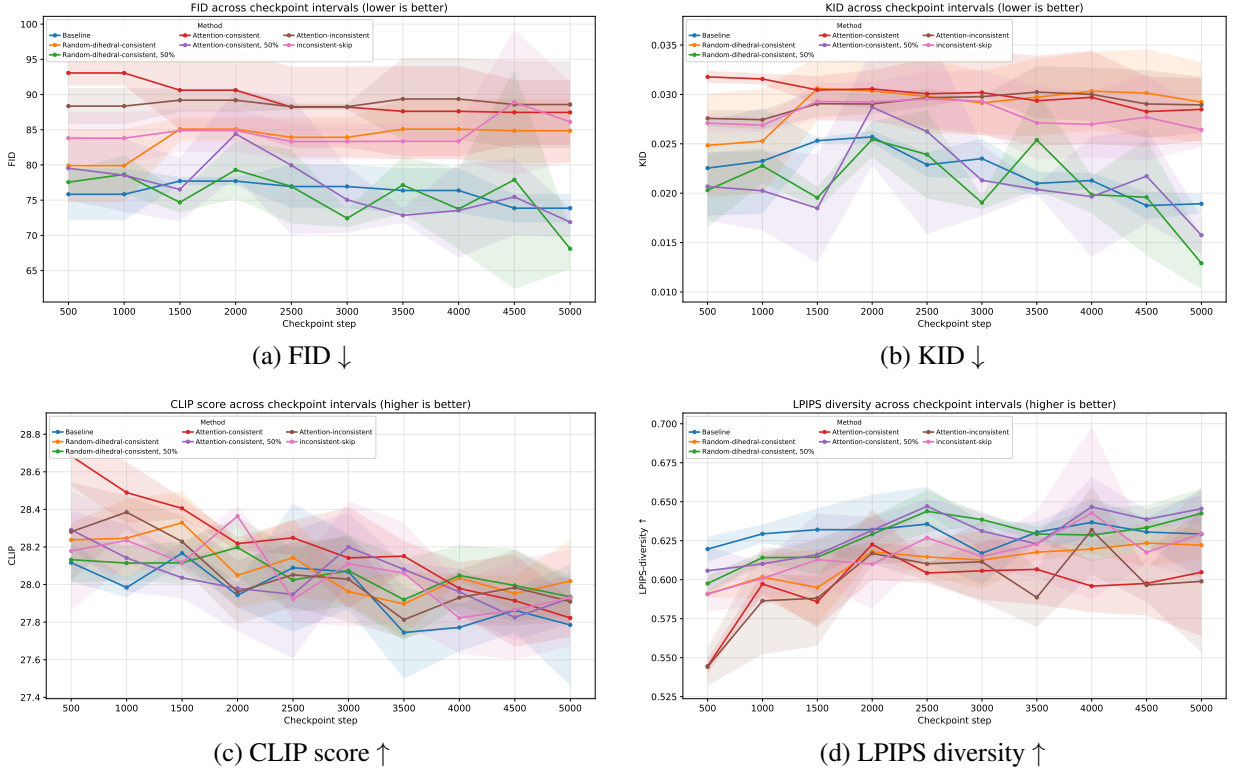


Figure 2: Image-level evaluation over 5,000 steps for seven modes and three seeds. Each mode–seed–checkpoint uses 500 images, totaling 105,000 images. Shading shows seed variability.

prediction error and should not be interpreted as image-space FID. We use it only as a practical fidelity signal for our controlled setting.

Self-Consistency Shift (SCS). Let A denote the clean feature map and \tilde{A} the feature map obtained under a transformation T . After aligning the intervened map back to the clean frame via $\tilde{A}^{\text{align}} = T^{-1}(\tilde{A})$, we define

$$\text{SCS} = \frac{1}{BCHW} \|A - \tilde{A}^{\text{align}}\|_1. \quad (19)$$

Lower SCS indicates stronger geometric self-consistency. The benefit of SCS is that it directly measures whether a symmetry-preserving intervention leaves the internal representation stable once the intended geometric transformation is factored out.

Activation Mass Scatter (AMS). For a feature map $A \in \mathbb{R}^{B \times C \times H \times W}$, let $m_b(h, w) = \sum_{c=1}^C |A_{b,c,h,w}|$ be the spatial activation mass for sample b , and let $\bar{m}_b(h, w) = \frac{m_b(h,w)}{\sum_{h,w} m_b(h,w)}$ be its normalized version. If $\mu_b \in \mathbb{R}^2$ denotes the center of mass of \bar{m}_b , we define

$$\text{AMS} = \frac{1}{B} \sum_{b=1}^B \sum_{h,w} \bar{m}_b(h, w) \|(h, w) - \mu_b\|_2^2. \quad (20)$$

Lower AMS indicates that activation mass is more spatially concentrated. The benefit of AMS is that it captures whether an intervention makes the representation more spatially organized or instead spreads activation mass more diffusely across the feature map.

Drift. Let μ_b and $\tilde{\mu}_b^{\text{align}}$ denote the centers of mass of the clean and aligned intervened activation maps, respectively. We define

$$\text{Drift} = \frac{1}{B} \sum_{b=1}^B \|\mu_b - \tilde{\mu}_b^{\text{align}}\|_2^2. \quad (21)$$

Lower Drift indicates stronger global spatial stability under intervention. Because it captures coarse displacement even when feature content remains similar, Drift complements SCS. Together, these metrics separate denoising fidelity from internal geometric stability: NP-MSE measures functional performance, whereas SCS, AMS, and Drift measure feature consistency, spatial spread, and global displacement. Additional details are provided in Appendix G.

4.3 MAIN RESULTS ON STABLE DIFFUSION U-NET

We evaluate all seven modes for 5,000 steps over three seeds to test whether hidden-state transformations preserve internal spatial stability, a behavior not isolated by input-level augmentation alone. Figure 1 reports NP-MSE, SCS, AMS, and Drift at 500-step intervals; lower is better for all four metrics. The 50% consistent variants give the best stability–fidelity trade-off, reducing geometry-sensitive metrics relative to full interventions and inconsistent controls while keeping NP-MSE competitive. We further report image-level FID, KID, CLIP score, and LPIPS diversity at the same checkpoints (Figure 2). For each mode, seed, and checkpoint, we generate 500 images, 250 cat-prompt and 250 dog-prompt, for 105,000 images total. The 50% consistent variants remain competitive on FID/KID while preserving comparable CLIP and LPIPS diversity, indicating that the internal stability gains do not degrade image-level quality or diversity. Random qualitative samples, selected uniformly from the full image pool, are provided in Appendix H.

4.4 PROOF-OF-CONCEPT FID COMPARISONS ON CIFAR-10, CELEBA-64, AND MNIST

To complement the main Stable Diffusion 2.1 study, we report small-scale proof-of-concept FID comparisons on CIFAR-10, CelebA-64, and MNIST. For CIFAR-10 and CelebA-64, we use the reproduced DDPM baselines of (Proszewska et al., 2025); for MNIST, we use the SDiT reference of (Yang et al., 2024). In all regularized variants, we keep the baseline architecture, diffusion objective, optimizer, sampling procedure, and evaluation pipeline fixed, and add only our regularization term.

In preliminary tuning, we found that applying the regularizer too rarely left training too close to the baseline, whereas applying it too frequently degraded performance. We therefore apply the regularization to a randomly selected half of the mini-batches during training. Table 1 reports the baseline references together with our measured regularized results under this 50% schedule. Additional dataset, training, and implementation details are provided in Appendix I. These results should be interpreted as proof-of-concept supporting comparisons under limited computational resources, rather than as definitive cross-dataset benchmark claims.

Table 1: Baseline references and measured regularized results. Lower FID is better. Regularized results are mean \pm std. over three runs for CIFAR-10 and MNIST, and two runs for CelebA-64.

Dataset	Model	Backbone	Resolution	FID \downarrow
CIFAR-10	Vanilla (Proszewska et al., 2025)	DDPM	32×32	4.46
CIFAR-10	Ours	DDPM	32×32	4.30 \pm 0.05
CelebA-64	Vanilla (Proszewska et al., 2025)	DDPM	64×64	4.51
CelebA-64	Ours	DDPM	64×64	4.53 \pm 0.33
MNIST	Vanilla (Yang et al., 2024)	SDiT	28×28	5.54
MNIST	Ours	SDiT	28×28	5.29 \pm 0.08

4.5 ADDITIONAL STUDIES

We complement the main U-Net study with supporting transformer-based analyses. The ViT experiments test geometric consistency in a simpler single-pass setting, while the DiT study illustrates why the same issue becomes more consequential in iterative denoisers.

4.5.1 ViT HIDDEN-STATE AUGMENTATION IMPROVES GENERALIZATION

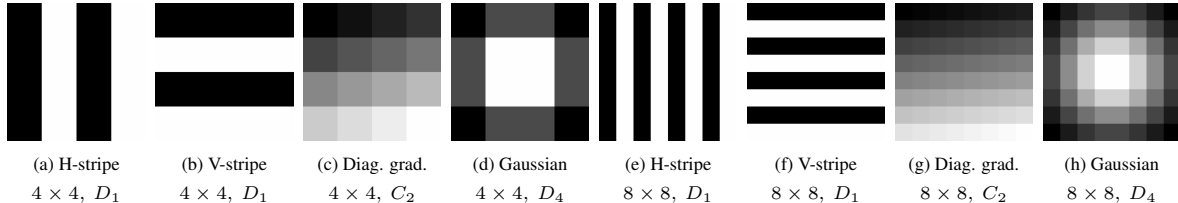
We study a pretrained ViT-B/16 (Dosovitskiy et al., 2021) on CIFAR-100 (Krizhevsky & Hinton, 2009) as a simple transformer testbed. We fine-tune it for five epochs under three settings: standard input augmentation at 224×224 , input augmentation at 384×384 , and our input-or-hidden (I/H) augmentation strategy, which applies reflection-based transformations either to the input or to intermediate hidden states. As shown in Table 2, I/H performs best, improving accuracy from 92.30% and 92.28% to 93.19%. This suggests that symmetry-aware hidden-state augmentation can already act as an effective regularizer in a standard ViT setting.

Table 2: ViT-B/16 classification accuracy on CIFAR-100. Higher is better.

Setting	Acc. (%)
Input aug. (224×224)	0.9230
Input aug. (384×384)	0.9228
Input/hidden aug. (224×224)	0.9319

Table 3: Synthetic probe consistency scores $S^{(5)}$.

Probe	4×4	8×8
H. stripe	0.570	0.548
V. stripe	0.581	0.523
Diag. grad.	0.624	0.650
Gaussian	1.000	1.000

Figure 3: **Synthetic symmetry probes with D_4 subgroup annotations.** Controlled probes for measuring geometric sensitivity and anisotropy in ViT attention under horizontal reflection.

4.5.2 SYNTHETIC AND REAL-IMAGE ATTENTION ANALYSIS

To examine the geometric effect of hidden-state flipping more directly, we consider both controlled synthetic probes and real-image attention visualizations. The synthetic probes isolate geometric structure, while the real-image study tests whether semantic behavior is preserved.

Synthetic probe evaluation. We construct synthetic inputs with explicit geometric structure, including horizontal and vertical stripes, diagonal gradients, and Gaussian-like blobs on 4×4 and 8×8 grids. Using a pretrained ViT-B/16, we compare the attention response of each probe to that of its horizontally flipped counterpart via

$$S^{(\ell)} = \frac{1}{M} \sum_{i=1}^M \text{cosine} \left(A^{(\ell)}(x_i), A^{(\ell)}(T(x_i)) \right), \quad (22)$$

where $A^{(\ell)}$ denotes the Block 5, Head 0 attention field and T is horizontal reflection. As shown in Table 3, stripe and gradient patterns achieve only moderate consistency, whereas Gaussian probes achieve perfect consistency. Together with Fig. 3, these results suggest that the selected ViT attention field responds more consistently to isotropic patterns than to directional ones under horizontal reflection, revealing measurable anisotropy.

Real-image attention perturbation. We next horizontally flip the Block 5 patch-token representation of a pretrained ViT-B/16 and propagate the modified state through the remaining encoder blocks. Figure 4 shows that the resulting attention remains focused on the same semantic object parts, but shifts to the mirrored location. Thus, for this selected attention field, the intervention alters spatial routing without disrupting semantic focus. In all qualitative visualizations, we report Head 0 of the selected transformer block; the rationale is provided in Appendix L.

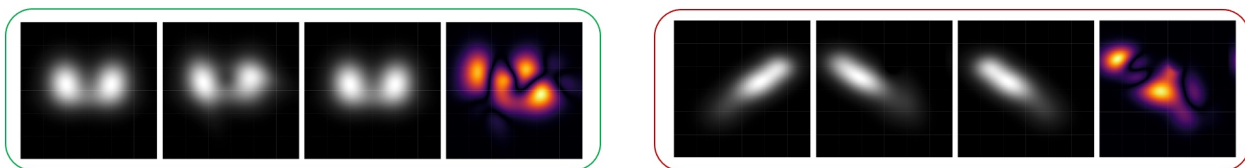
4.5.3 FLIPPED-HEAD ATTENTION IN DiT: QKV CONSISTENCY VS. MISMATCH

To connect the ViT analysis to Diffusion Transformers (DiTs), we perform a controlled synthetic experiment that isolates the geometric effect of hidden-state flipping inside attention. This is a controlled mechanistic analysis rather than a full DiT benchmark; it illustrates how geometric mismatch can become problematic when attention is applied repeatedly along the denoising trajectory.

We compare the two attention interventions defined earlier: the *attention-inconsistent* output-only flip of Eq. 5, and the *attention-consistent* reference corresponding to Eq. 6, implemented via coherent transformation of the interacting attention pathways. We consider both a symmetric and a non-symmetric synthetic baseline: the former tests geometric stability, while the latter tests geometric correctness under reflection. Figure 5 shows the same qualitative conclusion in both settings. Under the attention-consistent transformation, the attention field either preserves the baseline geometry (symmetric case) or yields the correct mirrored response (non-symmetric case). By contrast, the output-only flip produces shifted and distorted responses, because routing is computed in one coordinate frame while the resulting head output is interpreted in another. The distortion heatmap $|A_{\text{incon}} - A_{\text{con}}|$ makes this deviation explicit. These



Figure 4: **Hidden-state flipping in ViT-B/16.** From left to right: input image, original Block 5 Head 0 attention, attention after flipping the Block 5 patch-token hidden state, and the difference map $|A - \tilde{A}|$. The intervention preserves semantic focus while mirroring spatial routing.



(a) **Symmetric baseline.** A geometrically valid transformation should remain close to the reference pattern.

(b) **Non-symmetric baseline.** A geometrically valid transformation should produce the correct mirrored response.

Figure 5: **QKV consistency in flipped-head attention.** Symmetric and non-symmetric baselines isolate the geometric effect of hidden-state flipping. In each group, the panels show the baseline, the attention-inconsistent output-only flip, the attention-consistent QKV transformation, and the distortion heatmap $|A_{\text{incon}} - A_{\text{con}}|$. The consistent transformation preserves the expected geometry, whereas the output-only flip introduces visible distortion.

results illustrate the geometric-consistency principle: inside attention, a hidden-state transformation is stable only when all interacting pathways remain aligned in a common spatial frame. A minimal pseudocode implementation is provided in Appendix K.

5 CONCLUSION

We introduced a unified framework for *dihedral hidden-state interventions* and showed that *geometric consistency* determines whether such interventions stabilize or disrupt computation. Our main contributions are a common intervention formulation across convolutional and transformer-based architectures, a theoretical analysis of consistency in attention and U-Net fusion, and a geometry-aware evaluation suite based on SCS, AMS, Drift, and NP-MSE. Empirically, in our controlled Stable Diffusion 2.1 study, appropriately weighted consistent interventions improve hidden-state stability while preserving image-level quality. Supporting ViT and controlled DiT analyses show the same qualitative consistency principle. More broadly, these results suggest that geometric consistency is a useful design principle for symmetry-aware hidden-state adaptation, while leaving larger-scale studies and broader transformation sets to future work. Improved internal consistency, however, does not by itself address broader concerns such as bias, fairness, or misuse.

ACKNOWLEDGMENTS

This work was supported in part by funding from the Canada Excellence Research Chairs (CERC) program. The authors gratefully acknowledge this support. The authors also acknowledge Compute Canada and Calcul Québec for providing the computing resources used in this work.

REFERENCES

Peter L. Bartlett and Shahar Mendelson. Rademacher and gaussian complexities: Risk bounds and structural results. *Journal of Machine Learning Research*, 3:463–482, 2002.

- David Bau, Bolei Zhou, Aditya Khosla, Aude Oliva, and Antonio Torralba. Network dissection: Quantifying interpretability of deep visual representations. In *Proceedings of the IEEE Conference on Computer Vision and Pattern Recognition*, pp. 6541–6549, 2017.
- Hila Chefer, Shir Gur, and Lior Wolf. Transformer interpretability beyond attention visualization. In *Proceedings of the IEEE/CVF Conference on Computer Vision and Pattern Recognition*, pp. 782–791, 2021.
- Taco S. Cohen and Max Welling. Group equivariant convolutional networks. In *Proceedings of the 33rd International Conference on Machine Learning*, pp. 2990–2999, 2016.
- Zihang Dai, Fanpeng Meng, Moritz Maeurer, Yifan Chen, Yonatan Belinkov, and Iryna Gurevych. Knowledge neurons in pretrained transformers. In *Proceedings of the 38th International Conference on Machine Learning*, pp. 2702–2715, 2021.
- Alexey Dosovitskiy, Lucas Beyer, Alexander Kolesnikov, Dirk Weissenborn, Xiaohua Zhai, Thomas Unterthiner, Mostafa Dehghani, Matthias Minderer, Georg Heigold, Sylvain Gelly, Jakob Uszkoreit, and Neil Houlsby. An image is worth 16x16 words: Transformers for image recognition at scale. In *International Conference on Learning Representations*, 2021.
- Mojtaba Faramarzi, Mohammad Amini, Akilesh Badrinaaraayanan, Vikas Verma, and Sarath Chandar. Patchup: A feature-space block-level regularization technique for convolutional neural networks. In *Proceedings of the AAAI Conference on Artificial Intelligence*, volume 36, pp. 589–597, 2022.
- Marc Finzi, Samuel Stanton, Pavel Izmailov, and Andrew Gordon Wilson. Generalizing convolutional neural networks for equivariance to lie groups on arbitrary continuous data. In *International Conference on Learning Representations*, 2021.
- Mor Geva, Roei Schuster, Jonathan Berant, and Omer Levy. Transformer feed-forward layers are key-value memories. In *Proceedings of the 2021 Conference on Empirical Methods in Natural Language Processing*, pp. 5484–5495, 2021.
- Amir Hertz, Ron Mokady, Jay Tenenbaum, Kfir Aberman, Yael Pritch, and Daniel Cohen-Or. Prompt-to-prompt image editing with cross-attention control. *arXiv preprint arXiv:2208.01626*, 2022.
- Jonathan Ho, Ajay Jain, and Pieter Abbeel. Denoising diffusion probabilistic models. In *Advances in Neural Information Processing Systems*, volume 33, pp. 6840–6851, 2020.
- Emiel Hoogeboom, Victor Garcia Satorras, Clement Vignac, and Max Welling. Equivariant diffusion for molecule generation in 3d. In *Proceedings of the 39th International Conference on Machine Learning*, pp. 8867–8887, 2022.
- Edward J. Hu, Yelong Shen, Phillip Wallis, Zeyuan Allen-Zhu, Yuanzhi Li, Shean Wang, Lu Wang, and Weizhu Chen. LoRA: Low-rank adaptation of large language models. *arXiv preprint arXiv:2106.09685*, 2021.
- Alex Krizhevsky and Geoffrey Hinton. Learning multiple layers of features from tiny images. Technical report, University of Toronto, 2009. URL <https://www.cs.toronto.edu/~kriz/learning-features-2009-TR.pdf>.
- Kevin Meng, David Bau, Alex Andonian, and Yonatan Belinkov. Locating and editing factual associations in GPT. In *Advances in Neural Information Processing Systems*, volume 35, pp. 17359–17372, 2022.
- Omkar M. Parkhi, Andrea Vedaldi, Andrew Zisserman, and C. V. Jawahar. Cats and dogs. In *Proceedings of the IEEE Conference on Computer Vision and Pattern Recognition*, pp. 3498–3505, 2012.
- William Peebles and Saining Xie. Scalable diffusion models with transformers. In *Proceedings of the IEEE/CVF International Conference on Computer Vision*, pp. 4195–4205, 2023.
- Magdalena Proszewska, Nikolay Malkin, and N. Siddharth. On designing diffusion autoencoders for efficient generation and representation learning. *arXiv preprint arXiv:2506.00136*, 2025.
- Robin Rombach, Andreas Blattmann, Dominik Lorenz, Patrick Esser, and Björn Ommer. High-resolution image synthesis with latent diffusion models. In *Proceedings of the IEEE/CVF Conference on Computer Vision and Pattern Recognition*, pp. 10684–10695, 2022.
- Olaf Ronneberger, Philipp Fischer, and Thomas Brox. U-net: Convolutional networks for biomedical image segmentation. In *Medical Image Computing and Computer-Assisted Intervention*, pp. 234–241, 2015.

- Connor Shorten and Taghi M. Khoshgoftaar. A survey on image data augmentation for deep learning. *Journal of Big Data*, 6(1):60, 2019.
- Jiaming Song, Chenlin Meng, and Stefano Ermon. Denoising diffusion implicit models. In *International Conference on Learning Representations*, 2021a.
- Yang Song, Jascha Sohl-Dickstein, Diederik P. Kingma, Abhishek Kumar, Stefano Ermon, and Ben Poole. Score-based generative modeling through stochastic differential equations. In *International Conference on Learning Representations*, 2021b.
- Hugo Touvron, Matthieu Cord, Matthijs Douze, Francisco Massa, Alexandre Sablayrolles, and Hervé Jégou. Training data-efficient image transformers & distillation through attention. In *Proceedings of the 38th International Conference on Machine Learning*, pp. 10347–10357, 2021.
- Ashish Vaswani, Noam Shazeer, Niki Parmar, Jakob Uszkoreit, Llion Jones, Aidan N. Gomez, Łukasz Kaiser, and Illia Polosukhin. Attention is all you need. In *Advances in Neural Information Processing Systems*, volume 30, pp. 5998–6008, 2017.
- Maurice Weiler, Mario Geiger, Max Welling, Wouter Boomsma, and Taco S. Cohen. 3d steerable cnns: Learning rotationally equivariant features in volumetric data. In *Advances in Neural Information Processing Systems*, volume 31, 2018.
- Shu Yang, Hanzhi Ma, Chengting Yu, Aili Wang, and Er-Ping Li. SDiT: Spiking diffusion model with transformer. *arXiv preprint arXiv:2402.11588*, 2024.
- Sangdoon Yun, Dongyoon Han, Seong Joon Oh, Sanghyuk Chun, Junsuk Choe, and Youngjoon Yoo. Cutmix: Regularization strategy to train strong classifiers with localizable features. In *Proceedings of the IEEE/CVF International Conference on Computer Vision*, pp. 6023–6032, 2019.
- Hongyi Zhang, Moustapha Cisse, Yann N. Dauphin, and David Lopez-Paz. mixup: Beyond empirical risk minimization. In *International Conference on Learning Representations*, 2018.

APPENDIX

This appendix provides supplementary derivations, proofs, implementation details, and extended discussions supporting the main paper. We group the material into: (i) formal derivations for flipped-head interventions, (ii) extended consistency analysis for transformer denoisers, (iii) supplementary details for the Stable Diffusion UNet framework and experiments, and (iv) detailed definitions of the evaluation metrics.

A DETAILED DERIVATION OF FLIPPED-HEAD ATTENTION IN ViT

This appendix gives the index-level form of the flipped-head intervention used in the main text.

Let h^* be the selected attention head, and let

$$O_{h^*} \in \mathbb{R}^{N \times d_v}, \quad N = P^2.$$

Define the token-to-grid mapping

$$t(i, j) = (i - 1)P + j,$$

and reshape the head output into

$$O_{h^*} \in \mathbb{R}^{P \times P \times d_v}, \quad O_{h^*}[i, j, :] = O_{h^*}[t(i, j), :].$$

For a horizontal flip operator \mathcal{F} ,

$$(\mathcal{F}O_{h^*})[i, j, :] = O_{h^*}[i, P - j + 1, :].$$

Flattening back yields

$$\tilde{O}_{h^*}[t(i, j), :] = (\mathcal{F}O_{h^*})[i, j, :].$$

Replacing only head h^* gives

$$\hat{O} = \text{Concat}(O_1, \dots, O_{h^*-1}, \tilde{O}_{h^*}, O_{h^*+1}, \dots, O_H),$$

and the resulting block output is

$$Y = \widehat{O}W^O.$$

Equivalently, for token (i, j) ,

$$\mathbf{y}_{t(i,j)} = W^O \begin{bmatrix} O_1[t(i, j), :] \\ \vdots \\ O_{h^*-1}[t(i, j), :] \\ O_{h^*}[t(i, P-j+1), :] \\ O_{h^*+1}[t(i, j), :] \\ \vdots \\ O_H[t(i, j), :] \end{bmatrix}.$$

Thus, the intervention leaves the attention weights unchanged and modifies only the post-attention representation of one head, so each token mixes standard contextual features with a mirrored contextual feature from the transformed head.

B EXTENDED DIT CONSISTENCY ANALYSIS

This appendix provides additional justification for the consistency analysis introduced in Sec. 2.

B.1 PERMUTATION EQUIVARIANCE OF A SINGLE ATTENTION HEAD

Let

$$\mathcal{A}(Q, K, V) = \text{softmax}\left(\frac{QK^\top}{\sqrt{d_k}}\right)V$$

and let Π_T be the permutation matrix induced by a spatial transformation T on token indices. Then

$$\mathcal{A}(\Pi_T Q, \Pi_T K, \Pi_T V) = \Pi_T \mathcal{A}(Q, K, V).$$

Proof. Let

$$Q' = \Pi_T Q, \quad K' = \Pi_T K, \quad V' = \Pi_T V.$$

Then

$$Q'K'^\top = \Pi_T QK^\top \Pi_T^\top.$$

Since softmax is row-wise and commutes with simultaneous row/column permutations,

$$\text{softmax}(\Pi_T QK^\top \Pi_T^\top) = \Pi_T \text{softmax}(QK^\top) \Pi_T^\top.$$

Therefore

$$\mathcal{A}(Q', K', V') = \text{softmax}(Q'K'^\top)V' = \Pi_T \text{softmax}(QK^\top)V = \Pi_T \mathcal{A}(Q, K, V).$$

This shows that equivariance holds for an isolated transformed head. The inconsistency discussed in the main text therefore does not arise from the single-head attention map itself, but from mixing transformed and untransformed heads within the same multi-head block.

B.2 HEURISTIC ERROR PROPAGATION UNDER REPEATED ATTENTION PERTURBATIONS

We now give a heuristic linearized argument for why repeated denoising can amplify the effect of geometric inconsistency in transformer diffusion models.

Let

$$\tilde{O}_t = O_t + E_t,$$

where E_t denotes the perturbation induced by the inconsistent intervention at step t . Consider a schematic denoising update

$$z_{t-1} = \Psi_t(z_t, \hat{\epsilon}_t),$$

where $\hat{\epsilon}_t$ is the predicted noise and Ψ_t is the one-step sampler update. Linearizing with respect to the perturbation gives

$$\hat{\epsilon}_t^{\text{inc}} = \hat{\epsilon}_t + J_t E_t,$$

where $J_t = \partial \hat{\epsilon}_t / \partial O_t$ is the local Jacobian of the noise predictor with respect to the attention output. The resulting deviation in the denoising trajectory is approximately

$$\delta z_{t-1} \approx D_t J_t E_t,$$

where D_t is the local sensitivity of the sampler update to perturbations in the predicted noise. Unrolling across denoising steps yields the heuristic accumulation

$$\Delta_T \approx \sum_{t=1}^T D_t J_t E_t.$$

Thus, even small per-step geometric inconsistencies can accumulate into a nontrivial trajectory deviation over many denoising steps.

B.3 DIFFUSION TIMESTEP SENSITIVITY: ViT VS. DiT

For a ViT, attention is applied in a single forward pass. For a DiT, attention is applied repeatedly across denoising steps. Under the heuristic accumulation above, the relative sensitivity may scale with the number of denoising steps as

$$R = \frac{\|\Delta^{\text{DiT}}\|}{\|\Delta^{\text{ViT}}\|} \approx \frac{\sum_{t=1}^T \|D_t J_t E_t\|}{\|E_1\|}.$$

This suggests that repeated denoising can amplify the effect of geometric inconsistency more strongly in DiT than in a single-pass ViT.

C ADDITIONAL CLARIFICATION ON DIFFUSION HIDDEN-STATE INTERVENTIONS

The hidden-state intervention objective introduced in Sec. 2 applies unchanged to both U-Net and DiT diffusion backbones. For a sampled block ℓ and transformation $\tau \in \mathcal{T}$, we replace the original hidden activation

$$F^{(\ell)}(x_t, t)$$

by its transformed version

$$\tilde{F}^{(\ell)}(x_t, t) = \tau(F^{(\ell)}(x_t, t)),$$

and denote by $\varepsilon_{\theta}^{(\tau, \ell)}(x_t, t)$ the denoiser output of the modified network. The training objective then penalizes deviation between the target noise ε and the prediction $\varepsilon_{\theta}^{(\tau, \ell)}(x_t, t)$, as defined in Eq. 9.

What differs across architectures is not the objective itself, but the form of the coupled computation that must remain geometrically aligned. In U-Nets, the critical interaction arises at skip-connected encoder–decoder fusion: paired feature maps $F_{\text{enc}}^{(\ell)}$ and $F_{\text{dec}}^{(\ell')}$ at matched spatial resolution are combined through a fusion operator ϕ , so geometric consistency requires that both branches be expressed in the same transformed frame before fusion. In DiT-style denoisers, the corresponding interaction arises through attention and token mixing, as analyzed in Appendix B; there, consistency requires the interacting attention pathways to share a common transformed frame.

In our implementation, one intervention location ℓ and one transformation τ are sampled per mini-batch.

D PROOFS FOR SEC. 3

D.1 PROOF OF LEMMA 3.1

By construction, the reshaped head output satisfies

$$\mathcal{O}_{h^*}[i, j, :] = \mathcal{O}_{h^*}[t(i, j), :].$$

A horizontal flip acts as

$$(T\mathcal{O}_{h^*})[i, j, :] = \mathcal{O}_{h^*}[i, P - j + 1, :].$$

Flattening back defines

$$\tilde{\mathcal{O}}_{h^*}[t(i, j), :] = (T\mathcal{O}_{h^*})[i, j, :].$$

Substituting the flipped expression gives

$$\tilde{\mathcal{O}}_{h^*}[t(i, j), :] = \mathcal{O}_{h^*}[i, P - j + 1, :] = \mathcal{O}_{h^*}[t(i, P - j + 1), :],$$

which is exactly the claimed correspondence.

D.2 PROOF OF PROPOSITION 3.2

Let

$$\widehat{O} = \text{Concat}(O_1, \dots, O_{h^*-1}, \widetilde{O}_{h^*}, O_{h^*+1}, \dots, O_H)$$

denote the intervened multi-head representation. Partition the output projection as

$$W^O = [W_1^O \ \dots \ W_H^O], \quad W_h^O \in \mathbb{R}^{d_{\text{model}} \times d_v}.$$

Then for any token index t ,

$$\mathbf{y}_t = \sum_{h=1}^H W_h^O \widehat{o}_h[t],$$

where $\widehat{o}_h[t]$ is the token feature contributed by head h after the intervention. For $h \neq h^*$, we have

$$\widehat{o}_h[t(i, j)] = o_h[t(i, j)].$$

For the selected head, Lemma 3.1 gives

$$\widehat{o}_{h^*}[t(i, j)] = o_{h^*}[t(i, P - j + 1)].$$

Substituting these into the block expansion of $\mathbf{y}_{t(i, j)}$ yields

$$\mathbf{y}_{t(i, j)} = \sum_{h \neq h^*} W_h^O o_h[t(i, j)] + W_{h^*}^O o_{h^*}[t(i, P - j + 1)],$$

which proves the claim.

D.3 PROOF OF PROPOSITION 3.3

If every head output is transformed by the same permutation Π_T , then

$$Y_{\text{cons}} = \text{Concat}(\Pi_T O_1, \dots, \Pi_T O_H) W^O.$$

Because Π_T acts on the token axis while W^O acts on the concatenated feature axis, the permutation factors out:

$$\text{Concat}(\Pi_T O_1, \dots, \Pi_T O_H) = \Pi_T \text{Concat}(O_1, \dots, O_H).$$

Hence

$$Y_{\text{cons}} = \Pi_T \text{Concat}(O_1, \dots, O_H) W^O = \Pi_T Y.$$

Now suppose only a strict subset $S \subsetneq \{1, \dots, H\}$ of heads is transformed. Then the intervened output has the form

$$Y_{\text{partial}} = \text{Concat}(\widetilde{O}_1, \dots, \widetilde{O}_H) W^O, \quad \widetilde{O}_h = \begin{cases} \Pi_T O_h, & h \in S, \\ O_h, & h \notin S. \end{cases}$$

We claim that, in general, $Y_{\text{partial}} \neq \Pi_T Y$. To see this, it suffices to construct a counterexample. Choose some $h_0 \notin S$ and let all other head outputs be zero, while O_{h_0} is nonzero and not invariant under Π_T . Then

$$Y_{\text{partial}} = O_{h_0} W_{h_0}^O, \quad \Pi_T Y = \Pi_T (O_{h_0} W_{h_0}^O).$$

Since O_{h_0} is not invariant under Π_T , these two quantities differ in general. Therefore, selective transformation of only part of the multi-head module does not preserve a common transformed frame.

D.4 PROOF OF PROPOSITION 3.4

By assumption, the fusion operator ϕ is equivariant under simultaneous spatial permutation:

$$\phi(\Pi_T a, \Pi_T b) = \Pi_T \phi(a, b).$$

Applying this with

$$a = F_{\text{dec}}^{(\ell')} \quad \text{and} \quad b = F_{\text{enc}}^{(\ell)}$$

gives

$$\phi(\Pi_T F_{\text{dec}}^{(\ell')}, \Pi_T F_{\text{enc}}^{(\ell)}) = \Pi_T \phi(F_{\text{dec}}^{(\ell')}, F_{\text{enc}}^{(\ell)}),$$

which proves the consistency relation.

To see why one-sided transformation is inconsistent in general, consider a standard fusion operator such as addition:

$$\phi(a, b) = a + b.$$

Then

$$\phi(\Pi_T a, b) = \Pi_T a + b, \quad \Pi_T \phi(a, b) = \Pi_T a + \Pi_T b.$$

These are equal only in special cases, for example when $b = \Pi_T b$. Thus, applying the transformation to only one branch generally fails to preserve the common transformed frame. The same conclusion holds for common skip-fusion operations that depend nontrivially on both inputs, such as concatenation followed by a shared convolution.

D.5 PROOF OF THE SYMMETRY-REGULARIZATION CLAIM

Since $\mathcal{H}_{\text{sym}} \subseteq \mathcal{H}$, the supremum over \mathcal{H}_{sym} is bounded by the supremum over \mathcal{H} . Therefore, for any sample $S = \{x_i\}_{i=1}^n$,

$$\widehat{\mathcal{R}}_S(\mathcal{H}_{\text{sym}}) = \mathbb{E}_\sigma \left[\sup_{h \in \mathcal{H}_{\text{sym}}} \frac{1}{n} \sum_{i=1}^n \sigma_i h(x_i) \right] \leq \mathbb{E}_\sigma \left[\sup_{h \in \mathcal{H}} \frac{1}{n} \sum_{i=1}^n \sigma_i h(x_i) \right] = \widehat{\mathcal{R}}_S(\mathcal{H}).$$

Next, because $\mathcal{H}_{\text{sym}} \subseteq \mathcal{H}$, the induced loss classes satisfy

$$\mathcal{L}_{\mathcal{H}_{\text{sym}}} \subseteq \mathcal{L}_{\mathcal{H}}.$$

Applying the same monotonicity argument yields

$$\widehat{\mathcal{R}}_S(\mathcal{L}_{\mathcal{H}_{\text{sym}}}) \leq \widehat{\mathcal{R}}_S(\mathcal{L}_{\mathcal{H}}).$$

A standard Rademacher-complexity generalization bound for bounded losses then implies that applying the same bound to the symmetry-constrained subclass, equivalently to its induced loss class, yields a no-larger complexity term. This gives the claimed idealized regularization interpretation. The argument therefore shows only that the symmetry-constrained class has a no-larger Rademacher complexity term; it does not measure how tight or large the reduction is in a particular model class.

E STABLE DIFFUSION UNET FRAMEWORK

Our unified framework inserts exactly one sampled geometric transformation from the retained reflection subset at one selected location during each forward pass. Depending on the mode, candidate locations include ResNet blocks, attention blocks, and skip-connected fusion points.

E.1 INTERVENTION MODES

- **Baseline:** no intervention.
- **Random-dihedral-consistent:** the same sampled transformation is applied consistently across interacting pathways.
- **Attention-consistent:** the transformation is applied uniformly to Q , K , and V before attention.
- **Attention-inconsistent:** only the value projection or attention output is transformed.
- **Inconsistent-skip:** only one side of a skip connection is transformed.

E.2 ALGORITHM

Algorithm 1 summarizes the retained Stable Diffusion UNet training framework used in our experiments.

In Algorithm 1, $\text{APPLYINTERVENTION}(B, x, M, \tau)$ denotes the mode-specific operation at the sampled location. For random-dihedral-consistent, the sampled transformation is applied consistently across the interacting pathways at that location. For attention-consistent, the transformation is applied coherently inside attention (e.g. to the interacting attention pathways). For attention-inconsistent, only part of the attention computation is transformed.

This retained framework supports a controlled comparison of the implemented geometrically consistent intervention modes under a shared training protocol.

F STABLE DIFFUSION UNET EXPERIMENTAL DETAILS

We construct a lightweight but diverse experimental dataset by randomly sampling 500 images from the Oxford-IIIT Pet dataset Parkhi et al. (2012). All images are resized to 512×512 and encoded by the Stable Diffusion 2.1 VAE into latent tensors of shape $4 \times 64 \times 64$.

Algorithm 1 Schematic intervention framework for Stable Diffusion UNet**Require:** mode M , candidate sets $C_{\text{res}}, C_{\text{attn}}, C_{\text{skip}}$, transform set \mathcal{T}

```

1:
   
$$C \leftarrow \begin{cases} \emptyset, & M = \text{baseline}, \\ C_{\text{res}} \cup C_{\text{skip}}, & M = \text{random-dihedral-consistent}, \\ C_{\text{attn}}, & M = \text{attention-consistent}. \end{cases}$$

2: if  $C \neq \emptyset$  then
3:   Sample target block  $B^* \in C$ 
4:   Sample transformation  $\tau \sim \mathcal{T}$ 
5: end if
6: for each block  $B$  in the UNet do
7:   if  $M = \text{baseline}$  or  $B \neq B^*$  then
8:      $x \leftarrow B(x)$ 
9:   else
10:     $x \leftarrow \text{APPLYINTERVENTION}(B, x, M, \tau)$ 
11:   end if
12: end for
13: return output latent  $x$ 

```

F.1 TRAINING SETUP

Each experiment is run for 5,000 training steps. We use:

- batch size 4,
- AdamW optimizer with learning rate 10^{-5} ,
- a standard DDPM training scheduler,
- evaluation every 50 steps,
- final evaluation using full-UNet passes without intervention.

We keep all optimization and evaluation hyperparameters fixed across modes so that differences can be attributed to the intervention type rather than mode-specific tuning. The batch size and learning rate were chosen as a stable lightweight fine-tuning configuration for Stable Diffusion 2.1 under our GPU memory constraints. For the 50% variants, preliminary runs showed that applying the intervention too rarely stayed close to the baseline, whereas applying it to every minibatch could be overly strong; we therefore use a randomly selected 50% of minibatches as a fixed milder schedule.

F.2 REFLECTION TRANSFORM SET

For each forward pass, once a target layer is selected, we apply a randomly chosen reflection transformation from

$$\mathcal{T} = \{T_{\text{hor}}, T_{\text{ver}}, T_{\text{diag}}, T_{\text{anti}}\}.$$

We exclude rotations because VAE latents in Stable Diffusion are not reliably rotation-consistent.

F.3 RANDOM SELECTION OF AUGMENTATION LOCATION

Depending on the mode, augmentation is applied at exactly one randomly selected location during each forward pass:

- **ResNet modes:** candidates from down, mid, and up blocks.
- **Attention modes:** candidates include attention blocks.
- **Baseline mode:** no augmentation.

Sampling follows

$$B^* \sim \text{Uniform}(C), \quad \tau \sim \mathcal{T}.$$

F.4 WHY RANDOM LAYER SELECTION MATTERS

Stable Diffusion is hierarchical and spatially structured. Down blocks capture global geometry, mid blocks capture coarse semantics, and up blocks inject fine detail. Random perturbation location therefore:

- tests equivariance across multiple scales,
- avoids overfitting to a specific layer,
- exposes the network to geometric perturbations throughout its depth.

G METRIC DEFINITIONS AND IMPLEMENTATION DETAILS

This appendix specifies how the evaluation metrics in Sec. 4.2 are computed in practice.

Noise-Prediction Mean Squared Error (NP-MSE). We use

$$\text{NP-MSE} = \mathbb{E}_{x_t, t} [\|\hat{\varepsilon}_\theta(x_t, t) - \varepsilon\|_2^2]$$

as a lightweight fidelity proxy. This is simply the standard diffusion noise-prediction error averaged over evaluation samples and timesteps. We use *Noise-Prediction Mean Squared Error (NP-MSE)* as the direct name for this quantity; it should not be interpreted as an estimator of image-space Fréchet Inception Distance.

Feature alignment. For geometry-sensitive metrics, the clean activation is denoted by A and the intervened activation by \tilde{A} . When the intervention applies a transformation T , we first align the intervened activation back to the clean frame via

$$\tilde{A}^{\text{align}} = T^{-1}(\tilde{A}).$$

This ensures that SCS and Drift measure instability beyond the intended geometric transformation itself.

Self-Consistency Shift (SCS). After alignment, SCS is computed as

$$\text{SCS} = \frac{1}{BCHW} \|A - \tilde{A}^{\text{align}}\|_1.$$

This metric captures feature-level mismatch between clean and intervened representations after both are expressed in the same spatial frame.

Activation Mass Scatter (AMS). For each sample b , we define the spatial activation mass

$$m_b(h, w) = \sum_{c=1}^C |A_{b,c,h,w}|, \quad \tilde{m}_b(h, w) = \frac{m_b(h, w)}{\sum_{h,w} m_b(h, w)}.$$

Its center of mass is

$$\mu_b = \sum_{h,w} \tilde{m}_b(h, w) (h, w).$$

AMS is then defined as the second spatial moment of the normalized mass:

$$\text{AMS} = \frac{1}{B} \sum_{b=1}^B \sum_{h,w} \tilde{m}_b(h, w) \|(h, w) - \mu_b\|_2^2.$$

Thus AMS measures how spatially dispersed the activation mass is around its own center.

Drift. Let μ_b be the center of mass of the clean activation map and let $\tilde{\mu}_b^{\text{align}}$ be the center of mass of the aligned intervened activation map. Drift is defined by

$$\text{Drift} = \frac{1}{B} \sum_{b=1}^B \|\mu_b - \tilde{\mu}_b^{\text{align}}\|_2^2.$$

Unlike SCS, which measures feature-level difference, Drift captures whether the global spatial focus of the representation moves under intervention.

All hidden-state metrics are computed at the evaluated feature block and then averaged across the corresponding evaluation samples and timesteps.

H RANDOM QUALITATIVE SAMPLES

Random qualitative samples at checkpoint step 5000

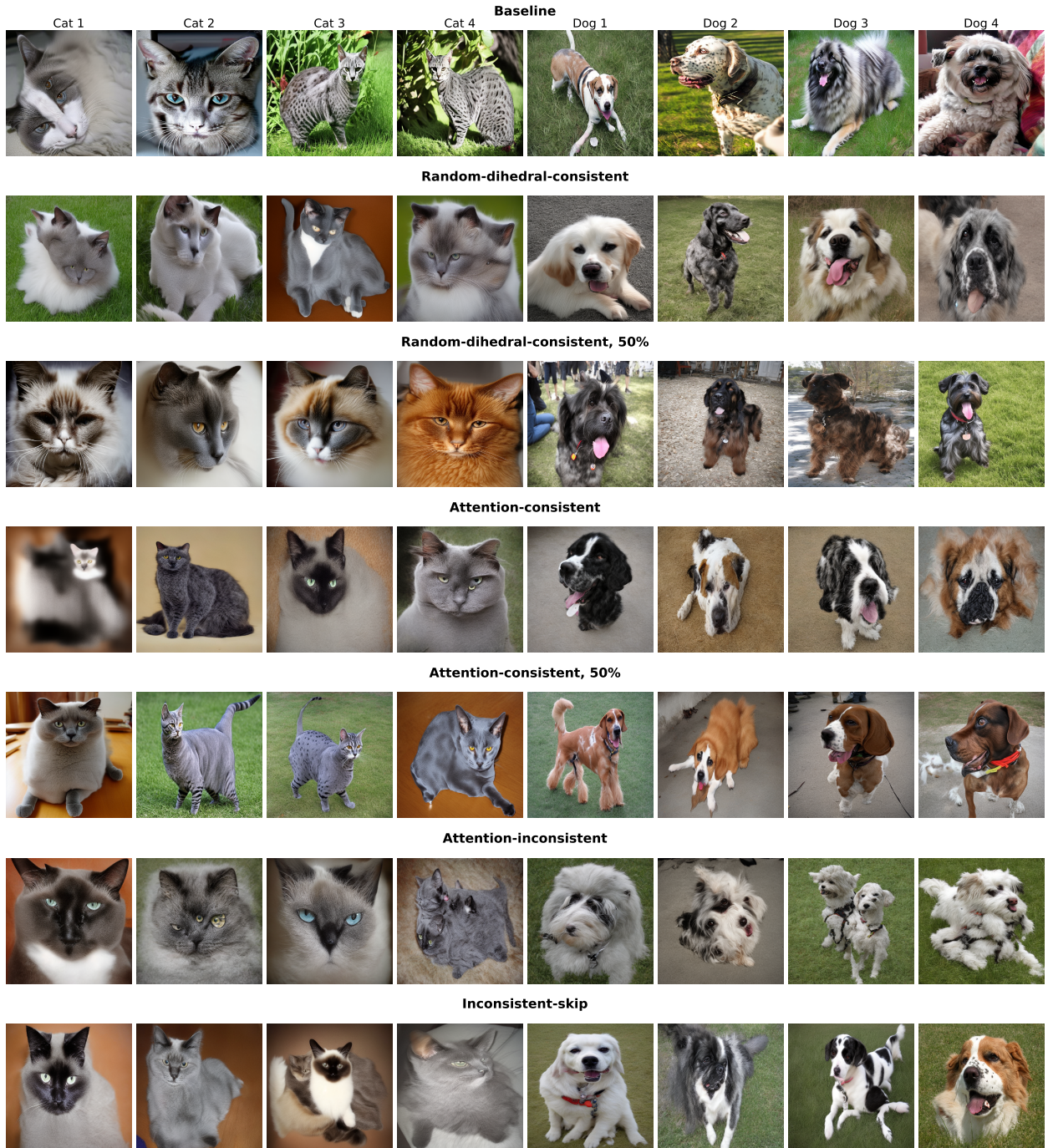


Figure 6: Random qualitative samples from the final checkpoint (5,000 steps). The examples were not manually curated; instead, they were sampled uniformly at random from the full set of 105,000 generated images. For each mode, we display four cat images and four dog images. Each row corresponds to one mode.

I PROOF-OF-CONCEPT FID COMPARISON DETAILS

This appendix provides additional dataset, reference, and training details for the proof-of-concept FID comparisons reported in Sec. 4.4.

I.1 DATASET CHOICE

Because these experiments are intended as small-scale supporting comparisons under limited computational resources, we restrict attention to compact and well-established datasets. CIFAR-10 and CelebA-64 serve as the main U-Net diffusion benchmarks, while MNIST provides a lightweight auxiliary transformer-based diffusion setting.

I.2 CIFAR-10 AND CELEBA-64 DDPM REFERENCES

For CIFAR-10 and CelebA-64, we use the reproduced vanilla DDPM baselines reported by Proszewska *et al.* Proszewska *et al.* (2025). For CIFAR-10, their setup uses 32×32 images, a cosine noise schedule, batch size 128, learning rate 10^{-4} , and 250K training iterations, reporting FID 4.46 at 100 denoising steps. For CelebA-64, the same source reports a reproduced DDPM baseline on 64×64 images with batch size 256, learning rate 10^{-4} , and 300K training iterations, yielding FID 4.51 at 100 denoising steps.

We use these reproduced values as our reference baselines because they provide a consistent protocol across both CIFAR-10 and CelebA-64.

I.3 AUXILIARY TRANSFORMER-BASED MNIST REFERENCE

To complement the U-Net baselines, we include an auxiliary transformer-based diffusion reference on MNIST using SDiT Yang *et al.* (2024). The paper reports FID 5.54 on MNIST at 28×28 resolution, evaluated using 50,000 real and 50,000 generated images. We treat this result as an auxiliary transformer-based reference rather than a directly matched DDPM baseline.

I.4 REGULARIZATION SCHEDULE

For all regularized variants, we keep the corresponding baseline architecture, diffusion objective, optimizer, sampling procedure, and evaluation protocol fixed, and add only our regularization term. In preliminary tuning, we found that applying the regularizer too rarely left training too close to the baseline, whereas applying it too frequently degraded performance. We therefore apply the regularization to a randomly selected 50% of mini-batches during training. This schedule provided the most reliable trade-off between preserving baseline dynamics and making the effect of the regularizer measurable in these small-scale experiments. Accordingly, these results are intended as supporting evidence under limited compute, rather than as definitive benchmark comparisons.

J ADDITIONAL ViT AND DiT STUDY DETAILS

This appendix provides brief setup details for the auxiliary ViT and DiT studies reported in Sec. 4.5.

J.1 ViT FINE-TUNING SETUP

For the ViT generalization study, we use a pretrained ViT-B/16 Dosovitskiy *et al.* (2021) and fine-tune it on CIFAR-100 Krizhevsky & Hinton (2009) for five epochs under three settings: (i) standard input augmentation at 224×224 , (ii) standard input augmentation at 384×384 , and (iii) input-or-hidden augmentation, in which reflection-based transformations are applied either to the input or to intermediate hidden states.

J.2 SYNTHETIC PROBE CONSTRUCTION

For the synthetic probe analysis, we use horizontal stripes, vertical stripes, diagonal gradients, and Gaussian-like blobs on 4×4 and 8×8 grids. These probes provide controlled geometric patterns with different symmetry properties, allowing us to test how consistently pretrained ViT attention responds under horizontal reflection.

The probe consistency score is computed as

$$S^{(\ell)} = \frac{1}{M} \sum_{i=1}^M \text{cosine}\left(A^{(\ell)}(x_i), A^{(\ell)}(T(x_i))\right),$$

where $A^{(\ell)}$ denotes the selected attention field and T is horizontal reflection.

J.3 DiT SYNTHETIC ATTENTION COMPARISON

For the DiT analysis, we compare two interventions inside attention: the output-only flip, which introduces QKV mismatch, and the QKV-consistent transformation, which preserves a common spatial frame. We evaluate both on a symmetric and a non-symmetric synthetic baseline to distinguish geometric stability from geometric correctness under reflection. A minimal pseudocode implementation is given in Appendix K.

K PSEUDO-CODE FOR THE FLIPPED-HEAD ATTENTION INTERVENTION

Algorithm 2 gives a minimal pseudocode view of the flipped-head intervention in attention.

Algorithm 2 Flipped-head intervention in multi-head attention

Require: query, key, value tensors Q, K, V ; selected head h^* ; spatial transformation T

- 1: **for** each head h **do**
 - 2: $O_h \leftarrow \text{softmax}(Q_h K_h^\top / \sqrt{d_k}) V_h$
 - 3: **end for**
 - 4: Reshape O_{h^*} to a spatial grid: $\mathcal{O}_{h^*} \in \mathbb{R}^{P \times P \times d_v}$
 - 5: Apply the transformation: $\tilde{\mathcal{O}}_{h^*} \leftarrow T(\mathcal{O}_{h^*})$
 - 6: Flatten back to token form: $\tilde{O}_{h^*} \in \mathbb{R}^{N \times d_v}$
 - 7: Replace the selected head output: $O_{h^*} \leftarrow \tilde{O}_{h^*}$
 - 8: Concatenate all heads and project:

$$Y \leftarrow \text{Concat}(O_1, \dots, O_H) W^O$$
 - 9: **return** Y
-

This pseudocode shows the output-only intervention used for the attention-inconsistent case. In the attention-consistent variant, the transformation is applied coherently to the interacting pathways before attention is computed.

K.1 GENERALIZATION TO OTHER HEADS

Although Head 0 is used as the primary visualization head in this work, the method is not restricted to it. The intervention can be applied to any head or block, and its effects propagate through deeper layers regardless of which head is selected for visualization.

L RATIONALE FOR SELECTING HEAD 0

In all qualitative ViT experiments and visualizations, we report attention maps using Head 0 of the selected transformer block (e.g., Block 5). This choice is based on our preliminary qualitative analysis.

L.1 INTERPRETABILITY OF HEAD 0

In our preliminary qualitative inspection, Head 0 exhibited comparatively compact and interpretable spatial patterns, making it a convenient choice for visualization:

- strong and compact activation on foreground objects,
- low background entropy,
- stable spatial localization across inputs,
- clear correspondence to human-interpretable regions.

This makes Head 0 particularly suitable for qualitative evaluation.